An overview of WFIRST-AFTA coronagraph modelling

John Krist, Bijan Nemati, Hanying Zhou, Erkin Sidick
Jet Propulsion Laboratory/California Institute of Technology,
4800 Oak Grove Drive, Pasadena, CA 91109 USA

ABSTRACT

The WFIRST/AFTA 2.4 m space telescope currently under study includes a stellar coronagraph for the imaging and spectral characterization of extrasolar planets. Based largely on performance predictions from end-to-end optical propagation modeling, promising coronagraphic methods were selected in late 2013 for further consideration for use on AFTA. Since those downselect analyses further modeling work has been done on evaluating refined coronagraph designs, wavefront sensing and control, detector representation, and time-dependent effects. Thermal, structural, ray trace, and diffraction propagation models are used in these studies. Presented here is the progress to date and plans for future analyses.

Keywords: WFIRST, AFTA, coronagraph

1. INTRODUCTION

NASA was given two 2.4 m diameter space-qualified telescope assemblies excessed by a reconnaissance program. One of these, the Astrophysics Focused Telescope Asset[1] (AFTA) has been designated for the NASA astrophysics program. The primary contender mission for it is the Wide Field Infra-Red Survey Telescope (WFIRST), which would search for signs of dark energy and also extrasolar planets via microlensing events. A coronagraph has been added to the baseline design for imaging and spectral characterization of extrasolar giant planets with contrasts of ~10^{-9} and circumstellar disks. While not optimized for coronagraphy, or even astronomy, the AFTA telescope is likely the best hope for a space-based, very-high-contrast coronagraph in the next decade.

The main drawback of AFTA for high contrast imaging is that it is an on-axis system with a central obscuration due to a secondary mirror that is supported by six fairly thick struts (Figure 1). These obscurations introduce considerable diffraction, and most coronagraphic methods do not perform well with them. Prior to AFTA most of the space coronagraph designs assumed a telescope optimized for exoplanet imaging with an off-axis, unobscured aperture. The potential for a mission by 2024 using AFTA spurred work on coronagraphs that could provide sufficient performance with the obscured aperture. Because time, facilities, and funding are limited, NASA formed the AFTA Coronagraph Working Group (ACWG) in 2013 to select those techniques that showed the best performance and likelihood of technological readiness. Due to the lack of testbed results with apertures like AFTA, numerical modelling was used to predict the performances of the contenders[2]. As described in a previous Proceedings, six coronagraphic techniques were evaluated: the Hybrid Lyot Coronagraph[3] (HLC), shaped pupil coronagraph[4] (SPC), phase-induced amplitude apodization with complex mask coronagraph[5] (PIAACMC), vector vortex coronagraph[6], and two versions of the visible nuller coronagraph[7,8]. At the end of 2013 the ACWG selected the HLC and SPC as the baseline design (they share the same optical layout), creating the Occulting Mask Coronagraph (OMC). The PIAACMC, which had high predicted performance but low technological readiness, was selected as a backup, with lower priority for funding and testbed time.

Since the downselect, all three techniques have been further optimized to provide better contrast, inner working angle, throughput, and reduced sensitivity to aberrations. We present here the predicted performance of the latest flight coronagraph designs.

2. CORONAGRAPH OVERVIEW

The current AFTA coronagraph baseline design (Figure 2) begins with a set of fold mirrors that divert the beam from the secondary into the coronagraph. Collimating optics create a pupil image on an actuated tip/tilt mirror (the fast steering mirror or FSM) that corrects body pointing errors. More optics create another pupil image on a 48 x 48 actuator deformable mirror (DM). Another identical DM is situated 1 meter downstream, and the two DMs together provide both

phase and amplitude wavefront control over a 360° field around the star[9]. After the DMs another pupil image is formed on a selectable fold mirror on which the shaped pupil mask pattern is deposited (a plain fold is used with the HLC). The beam is then focused onto a focal plane mask (FPM). A variety of SPC and HLC FPMs can be selected using a wheel mechanism. Another pupil image is then created in the plane of the Lyot stop. The beam is again brought to focus for a field stop that is used to block bright light outside the region of interest to prevent detector saturation and scattering by the backend optics. After that a selectable mirror switches between an integral field spectrograph (IFS) or an imaging channel. In each channel a filter wheel provides a variety of bandpasses. The IFS works over 600 - 950 nm with a resolution of R = 70 and the imager from 400 - 800 nm. In the imaging channel a polarizing beamsplitter creates orthogonal polarization images simultaneously on the same CCD detector. Excluding the IFS, there are 31 reflections in the system, including the telescope optics. The PIAACMC requires a slightly different layout due to the need for the PIAA optics to apodize the beam and to accommodate multiple-plane Lyot stops. At the specification of the designer, only a single DM is used in the PIAACMC layout to simplify the system (this allows control over one-half of the field around the star).

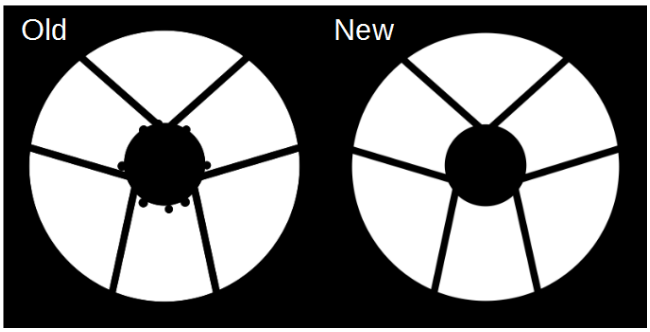

Figure 1. The AFTA telescope obscuration pattern. The "old" pattern on the left includes metrology markers along the edge of the secondary obscuration. Because the primary and secondary mirrors will be refigured and recoated, these will be removed so that the pupil will look like the "new" pattern on the right. All of the coronagraph designs presented here are for the "old" pattern except for the revised PIAACMC, which uses the new one (the markers do not significantly affect the performance either way).

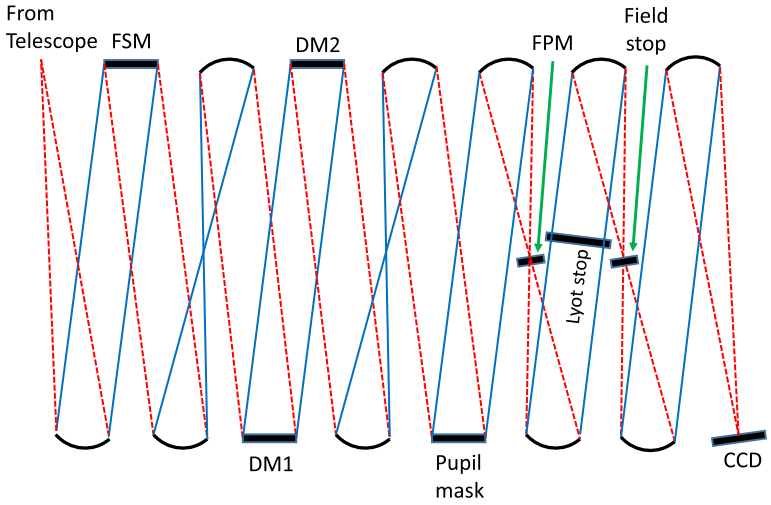

Figure 2. Conceptual layout of the post-downselect Occulting Mask Coronagraph composed of the shaped pupil and hybrid Lyot coronagraphs. Fold mirrors are not shown. In color in the online proceedings.

A low order wavefront sensor[10] (LOWFS) is used to measure time-varying low order aberrations such as pointing errors, focus, coma, astigmatism, etc. Pointing errors are corrected by the FSM at a rate of ~2 kHz and focus by a piston-actuated optic at intervals of tens or hundreds of seconds. The other aberrations are expected to be controlled using the deformable mirror at intervals of ~1000 sec. In the SPC and HLC the FPMs are reflective and will have patterned dielectric coatings to create a tailored phase modulation in the reflected image of the PSF core that is fed into a Zernike phase contrast sensor. In PIAACMC the Lyot stop is reflective and diverts the rejected light onto a detector, creating a defocused image. In either case modes corresponding to Zernikes are fit to the time-differenced LOWFS images to determine the wavefront change. The FSM, focus corrector, and DM are then set to stabilize the wavefront.

3. MODELLING AND EVALUATION PROCEDURE

As with the downselect process, the revised coronagraph designs were evaluated using end-to-end numerical wavefront propagation modelling in a realistically aberrated system with wavefront control provided by deformable mirrors. An unfolded layout containing all of the optical elements of the telescope and coronagraph was created using the PROPER propagation library[11,12]. Each surface had realistic phase and amplitude errors defined by power spectral density (PSD) specifications. PROPER propagated the wavefront from surface to surface using angular spectrum and Fresnel algorithms, picking up the aberrations along the way. Broadband images were generated using 9 monochromatic images spanning the passband averaged together. The coronagraphs were represented as phase and/or amplitude modifications to the wavefront. In cases where a coronagraphic component could not be well represented using the provided PROPER routines (the small PIAACMC focal plane mask, for instance), additional custom code was developed. These special cases, such as using a matrix Fourier transform for the PIAACMC mask, are detailed in the previous Proceedings[2].

The coronagraph suppresses the diffraction pattern but not the scattered light from the optical aberrations. These were reduced in the simulations using wavefront control with the deformable mirrors (PROPER includes a deformable mirror model with actuator influence functions). The DM settings required to create a dark hole around the star were determined using the Electric Field Conjugation[13] (EFC) method, which uses the sensed complex image plane field along with the predicted DM image plane response. Unless otherwise noted, the computed image plane field was directly used rather than sensed (which would be done by putting predefined patterns on the DM and measuring the image plane intensity changes[14]).

The fast AFTA primary mirror creates polarization-induced aberrations, primarily astigmatism, that have a significant impact on the performance of a coronagraph. Because PROPER does not do any ray tracing or accounts directly for coating properties, these aberrations are computed using Zemax for orthogonal polarizations and added to the PROPER model as wavelength-dependent wavefront errors. The EFC wavefront control procedure can then be used to optimize for a single polarization channel or provide a compromise solution for both channels (which is also generally the equivalent of not having a polarization-split imager). Note that the unlike the imaging channel, IFS does not have split polarizations.

After the dark hole was generated the effects of pointing jitter were computed. This was done by creating image plane intensity fields for many offsets of the source (via wavefront tip/tilt) that were then added together with weights representing a two-dimensional Gaussian distribution. For the cases evaluated here, the pointing jitter (after correction by the fast steering mirror) was 0.4, 0.8, and 1.6 milliarcseconds RMS per axis (this is the current expected range of post-correction pointing jitter).

Other aspects of the coronagraph were also computed. The field (planet) PSF may be field dependent (PIAACMC) or have low core flux due to scattering of light into the PSF wings (HLC, SPC). The field PSF was computed for different radial offsets by propagating a wavefront tilt through the system. Properties such as the fraction of a planet's light entering the telescope that falls within the full-width-at-half-maximum region of the core (*PSF core throughput*) and the area of that region (*PSF core area*) were derived. The sensitivity of each coronagraph to low order aberration changes was also computed by separately propagating specific Zernike polynomial wavefront errors through the system and measuring the image plane field change.

4. HYBRID LYOT CORONAGRAPH

The HLC (Figure 3) is a modification of the classical Lyot coronagraph that consists of an occulting mask located at an intermediate focal plane and a pupil mask at a subsequent pupil plane. In the HLC the focal plane mask (FPM) is a combination of a patterned amplitude modulator (a metal coating) with an overlaid phase modulator (a patterned

dielectric coating). Both are simultaneously optimized to provide an acceptable compromise in IWA, contrast, bandwidth, low-order aberration tolerance, and throughput, with the wavelength-dependent characteristics of the materials included. The phase-and-amplitude modulating FPM provides better performance over broad bandpasses than previous amplitude-only designs.

Like most coronagraphic techniques the performance of the HLC is seriously impacted by obscurations in the telescope, especially the spiders. As part of the design optimization process the DMs are used to alter the wavefront to reduce the obscurations' diffractive effects. Pointing jitter is also included in the optimization. The resulting complicated pattern of actuator pistons has relatively large strokes (>200 nm), introducing about a wave of peak-to-valley phase error. These patterns are an inherent part of the HLC diffraction suppression and would be used whether there were aberrations in the system or not. The large intentional wavefront errors, while improving contrast, do significantly degrade the field point spread function, scattering light from the core into the wings. Thus, the HLC has a fairly low PSF core throughput, more pronounced than would be expected simply from the loss of light at the Lyot stop. Beam walk on the second, non-pupil DM caused by pointing offsets also introduces a small field dependence in the PSF.

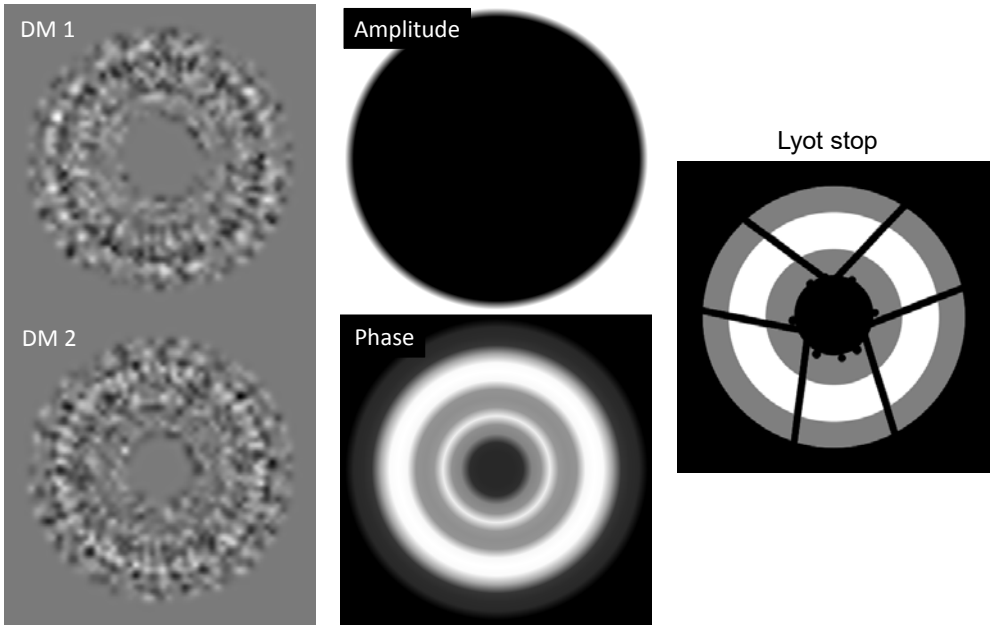

Figure 3. Revised HLC components: (left) DM wavefront error patterns (497 nm peak-to-valley); (middle) focal plane mask phase and amplitude modulation patterns at λ = 550 nm (6 λ/D on a side); (right) Lyot stop pattern (grey) superposed on the AFTA obscuration pattern (black). The central spot in the FPM phase is intended for use by the Zernike phase contrast low order wavefront sensor.

Substantial optimization of the HLC design was made after the downselect with the goal of improving jitter tolerance, decreasing the IWA, reducing FPM complexity, and reducing DM stroke. At the same time, the dielectric coating on the FPM was constrained so that the rejected PSF core light reflected by the metallic coating underneath it would have a suitable phase modulation for input into a Zernike phase contrast low-order wavefront sensor. The revised HLC design (HLC 20140623-139) operates over a 523 - 578 nm bandpass (λ_c = 550 nm) with an r = 3.0 - 10.5 λ_c/D, 360° dark hole field defined by the DM patterns. The FPM has a solid r = 2.6 λ_c/D occulting spot with partial (~0.05%) intensity transmission, and the dielectric pattern does not extend beyond this radius.

The DM surface deformations have been reduced by about a factor of two from the downselect design to a peak-to-valley range of 248 nm. With the lower DM strokes the field PSF is sharper than the downselect design. The PSF core throughput is now 4.3% (AFTA without a coronagraph would be 34%), and the core area is 2100 mas^2. The IWA is 3.0 λ_c/D.

The HLC results are shown in Figure 4. With system aberrations EFC produces a mean contrast in a single polarization of 6×10^{-10} from $r = 3$ - 4 λ_c/D and 3×10^{-10} from $r = 3$ - 10 λ_c/D. When this solution is evaluated for the orthogonal polarization, the contrast is about 6× worse (the difference would be greater in passbands longer or shorter of 550 nm due to the increase in the polarization-induced wavefront error). Optimized for both polarizations the mean contrasts are about 2 - 3 times higher, so it may be practical to observe simultaneously in both polarization at once in the 523 - 578 nm bandpass without a huge signal-to-noise loss over a single polarization.

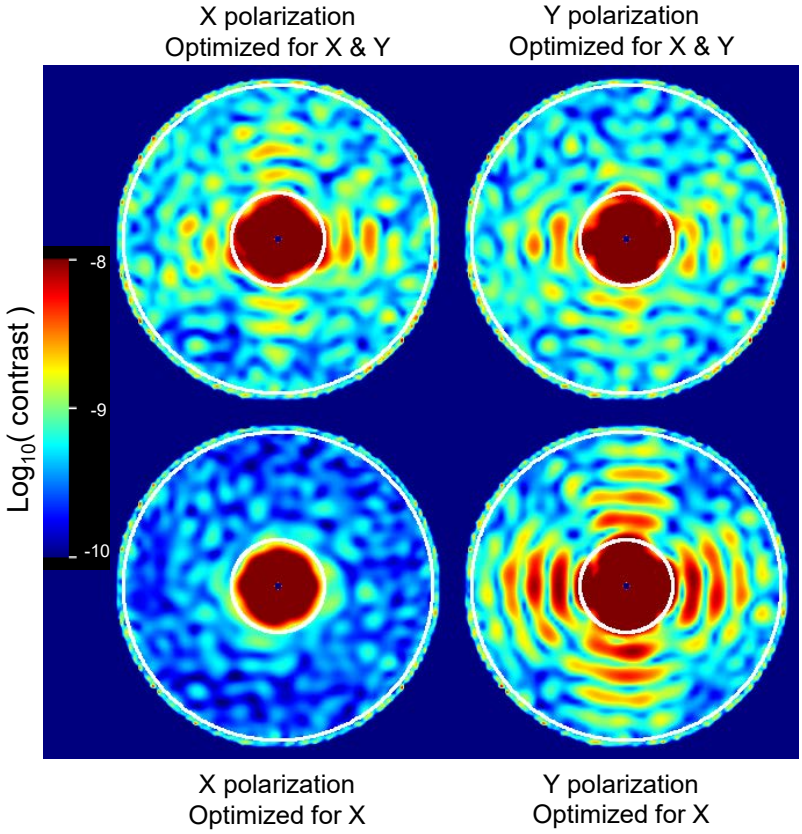

Figure 4. Revised HLC maps (λ = 523 - 578 nm; λ_c = 550 nm) for the aberrated system showing post-EFC contrast with 0.4 mas RMS jitter and 1.0 mas star in the X and Y polarization channels when EFC was optimized for (top) for both polarizations and (bottom) for only the X polarization. The cross-shaped patterns are due to the difference in astigmatism between the two polarization axes. Circles are $r = 3$ & 10 λ_c/D. In color in the online proceedings.

Note that the speckle patterns are different in the two polarization channels when EFC optimizes for both. On ground-based telescopes, with poorer contrast and where the instrumental polarization signature is not as dominant, the speckle patterns look the same in both polarizations, and simultaneous observations in both channels are used to distinguish polarized sky sources (primarily dust disks) from the background speckles. This will not be possible with any AFTA coronagraph.

When pointing jitter is added to the single polarization solution (Figure 5) the contrast degradation is fairly low up to 0.8 mas RMS. With 1.6 mas RMS of jitter the contrast is about 7× worse at the IWA than the no-jitter case. However, at r = 4 λ_c/D its contrast is 7× better than the downselect design. The revised HLC has a nearly order of magnitude improvement in the tip/tilt and astigmatism tolerance at 3 λ_c/D relative to the downselect HLC.

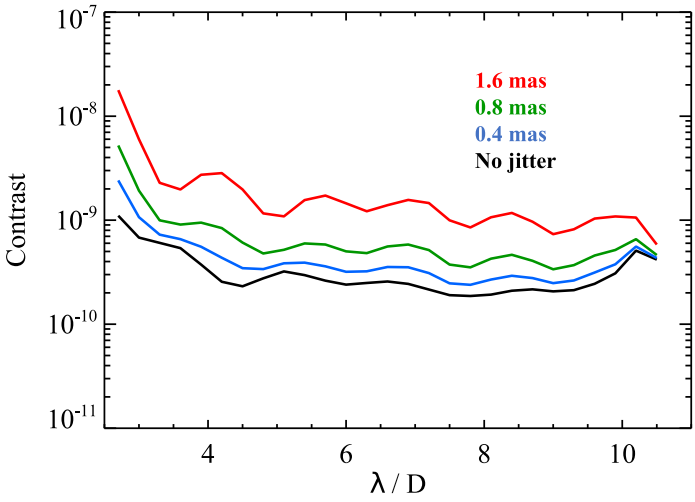

Figure 5. Revised HLC (λ = 523 - 578 nm; λ_c = 550 nm) mean azimuthal contrast versus field radius with different levels of jitter and (for jittered results) 1.0 mas star evaluated in and optimized for the X polarization channel. In color in the online proceedings.

5. SHAPED PUPIL CORONAGRAPH

The SPC uses a binary pupil mask with tailored openings that control the pattern of diffracted light, distributing it outside of a desired dark hole region. The telescope obscurations are masked out as part of the design. The minimum IWA and best contrast that can be achieved are dependent on the size of the dark hole and the transmission loss that is considered acceptable. An advantage of a pure shaped pupil mask like that used in the downselect design is that it is very insensitive to low order aberration changes, especially pointing errors (these simply cause an offset of the diffraction pattern, including the dark hole, but do not alter the contrast inside the hole). It is also achromatic, allowing it to be used over a broad bandpass, though the size of the diffraction pattern scales with wavelength. The downsides of the shaped pupil are its low transmission and broad field PSFs. Because of its large bandwidth it has been baselined for use with the integral field spectrograph in the current AFTA design studies. A variety of shaped pupils can be used to create dark fields in different areas. A "characterization" shaped pupil, intended for use with the IFS, provides the best IWA but at the cost of a limited OWA and azimuthal field coverage. Another mask intended for disk imaging creates a 360° dark field with a large OWA but also with a larger IWA.

After the pure shaped pupil design was chosen in the downselect it was found that by adding a Lyot stop at a pupil after the field stop the performance could be improved, including having a smaller IWA. This configuration is somewhat analogous to the Apodized Pupil Lyot Coronagraph, but with a different apodization form. A large fraction of diffracted light that passes through the field stop gets concentrated inside the central obscuration and outside the aperture as viewed at the reimaged pupil. The Lyot stop there is simply an annulus blocking the inner and outer obscurations, with some oversizing. The shaped pupil is optimized for given field and Lyot stops. There are two current flight designs: the characterization mask (identified as SPC 20140902-1) provides an r = 2.5 - 9 λ_c/D field over two 65° opening angle sectors on opposing sides of the star over an 18% bandpass, while a disk imaging mask (SPC 20141007) provides a 360° field from r = 6.5 - 20 λ_c/D over a 10% bandpass and is intended for circumstellar disk imaging. In both cases the dark hole regions are defined by hard-edge field stops. Only the characterization SPC (Figure 6) is discussed here.

The characterization SPC produces a field PSF with a FWHM area of 2600 mas^2 and a PSF core throughput of 3.7%. A considerable fraction of the light is diffracted to large angles by the mask. The IWA is r = 2.8 λ/D. The mean contrast over an 18% bandpass (λ = 728 - 872 nm, λ_c = 800 nm) in an unaberrated system is 4 × 10^{-9} over the full dark hole field and 1 × 10^{-8} between r = 2.5 - 3.5 λ_c/D. To see what additional gain in diffraction suppression that wavefront control could provide EFC was run on this SPC in the unaberrated system using the two DMs. At the suggestion of the SPC designers the region between 2.5 - 4.5 λ_c/D was given 5× greater weighting than the rest of the dark hole to force EFC to provide a solution better optimized for contrast at the IWA. This improved the mean contrast over the full dark hole to 2 × 10^{-9} over the field and between r = 2.5 - 3.5 λ_c/D.

Figure 6. (Left) SPC characterization pupil mask. (Right) SPC occulter/field stop (r = 2.5 - 9 λ_c/D).

The unaberrated system EFC DM solutions were used as the starting point for another run of EFC in which the aberrations were included and the X and Y polarizations were optimized together (Figure 7). Again, field-dependent weights were applied. EFC converged to a mean contrast of 4×10^{-9} over the full dark hole field and 6×10^{-9} between r = 2.5 - 3.5 λ_c/D. As an experiment, EFC was run again optimizing and evaluating only the X polarization image, and the result was about 30% lower than the dual polarization values, close to the unaberrated contrasts. This shows that the contrast limit is primarily set by the shaped pupil and the polarization-induced aberrations rather than the optical fabrication errors.

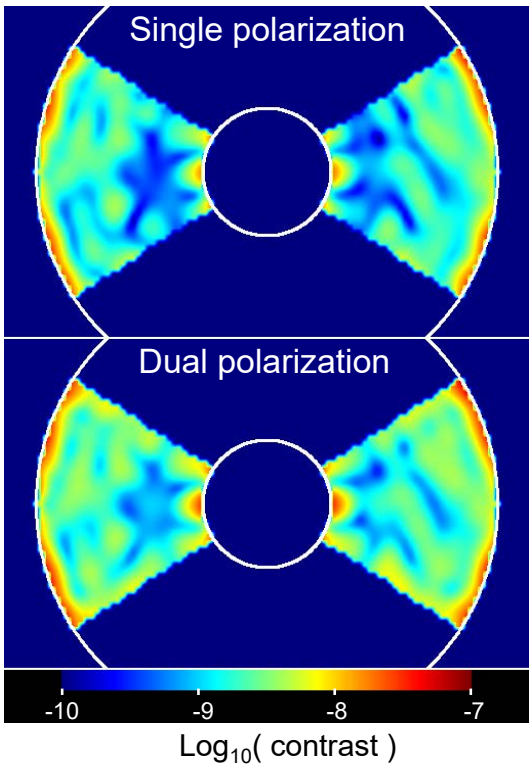

Figure 7. Contrast maps for the revised shaped pupil (λ = 728 - 872 nm, λ_c = 800 nm) after running EFC when (top) optimized for a single polarization, and (bottom) optimized for both. The circles indicate r = 2.5 & 9.0 λ_c/D. No jitter has been added. In color in the online proceedings.

The addition of jitter to the dual polarization solution shows a relative insensitivity to pointing. Compared to no jitter, the contrast degrades by about 50% with 1.6 mas RMS of jitter (Fig. 13). The SPC has a high tolerance of pointing (tip/tilt) and, important for polarization, astigmatism errors. It is most sensitive to coma and spherical aberration while being moderately sensitive to focus and trefoil. Its broad bandwidth and low sensitivity to pointing and polarization-induced aberrations make this SPC a good match to the long wavelength IFS (the polarization-induced aberrations increase at wavelengths longer or shorter than 550 nm).

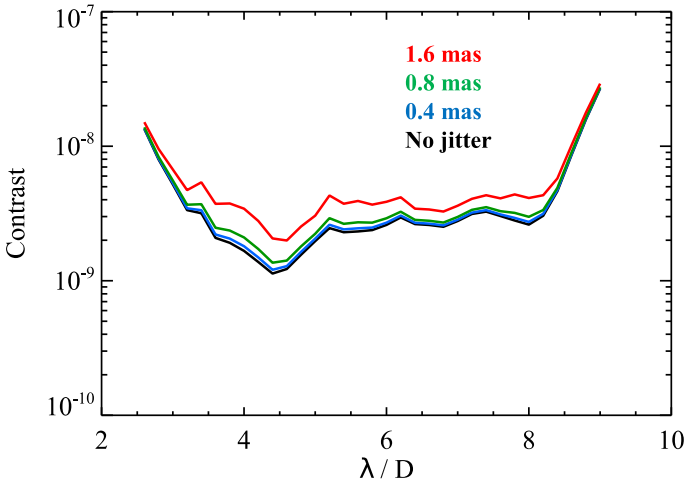

Figure 8. Revised shaped pupil radial mean contrast optimized for dual polarization (λ = 728 - 872 nm) with different amounts of RMS jitter (non-zero jitter results also include a 1.0 mas diameter star) added to the EFC solution. In color in the online proceedings.

6. PHASE INDUCED AMPLITUDE APODIZATION COMPLEX MASK CORONAGRAPH

The PIAACMC combines the nearly lossless beam apodization of a classical PIAA coronagraph with a focal plane phase mask. A PIAA coronagraph relies on a pair of optics: the first (M1) compresses the beam into the desired pupil apodization profile and the second (M2) corrects for path length errors introduced by the remapping. After propagation to an intermediate focus the resulting PSF has a broadened core containing most of the light and significantly reduced wings. In the classical PIAA an opaque occulting spot is used to block the bulk of the starlight residing in the core, providing a high contrast field. The wavefront remapping results in a significant off-axis comatic distortion of the field PSF, so a reverse set of PIAA optics undistorts the wavefront, providing a sharp final PSF. The advantages of PIAA are a small IWA (a result of the magnification from the remapping) and high throughput (the apodization is done via beam reshaping rather than altering the transmission pattern with an absorbing mask). The classical PIAA, however, is not tolerant of an obscuration pattern like AFTA's, resulting in unacceptably poor contrast.

The PIAACMC variation (Figure 9) replaces the opaque spot at focus with a small phase-modulating mask (the complex-mask, CM, part of PIAACMC) and uses much weaker PIAA optics. In the monochromatic case, the mask covers a portion of the stellar PSF core and shifts its phase relative to the rest of the PSF. As the beam propagates to a subsequent pupil interference causes starlight to diffract outside of the pupil as well as into the shadows of any obscurations where it is blocked by a Lyot stop. Because the bulk of the diffraction suppression is done by the phase mask, the apodization provided by the PIAA optics here is much less aggressive, making the optical surfaces easier to fabricate. Whereas a classical PIAA system may provide magnifications in the focal plane of 3× – 5×, the PIAACMC optics have magnifications more like 1.2×. As with a classical PIAA coronagraph reverse remapping optics can restore the wavefront distortion introduced during the apodization, but the less severe wavefront remapping of PIAACMC results in a fairly weak field dependence in the PSF, and they may be omitted for limited OWAs. In the absence of reverse optics the reimaged pupil after the FPM is not planar - different parts of the pupil are in focus at different

locations along the optical axis. In this case there are multiple Lyot stops along the axis, each masking only those portions of the images of the obscurations that are in or near focus at each plane.

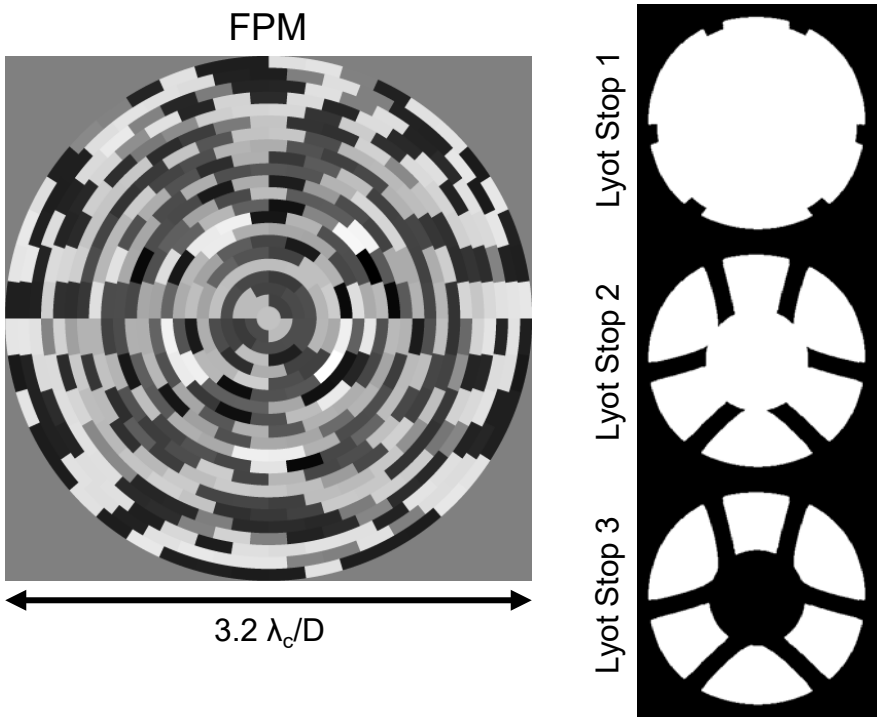

Figure 9. Revised PIAACMC focal plane mask surface height map and Lyot stops. The barrel distortion seen in the Lyot stop spider patterns is due to the remapping of the beam by the PIAA optics.

A simple phase mask consisting of a uniform-height spot of a suitable material (e.g., dielectric) works in monochromatic light, but in broadband the wavelength dependence of the phase shift, wavelength dispersion of the material, and the size dependence of the PSF necessitates a more complex solution. One method is to construct the phase mask with multiple concentric rings of material with different thicknesses optimized to provide the required contrast over a given bandpass. The joint optimization of the PIAA optics and these rings is complicated and numerically intensive, and it may include pointing error and other low order wavefront error tolerancing as constraints.

As with the downselect version, the current design (PIAACMC 20150322) includes weak PIAA optics, a focal plane phase mask, and multiple Lyot stops, but it dispenses with the reverse PIAA optics and the backend Lyot coronagraph. An additional simplification is the use of a single DM for wavefront control, limiting the dark hole to one-half the area that would be possible with two DMs. The PIAA optics are now circularly symmetric (except for the off-axis component that is not included in the PROPER modelling and which may itself be eliminated using on-axis optics). The specified operating bandpass of this design is 523 - 578 nm (λ_c = 550 nm). The phase mask is now a 3.2 λ_c/D diameter series of 22 concentric rings with azimuthal sectors of various heights (-339 to +355 nm) on a reflective surface. The addition of the azimuthal variations allows for more degrees of freedom for improving the bandwidth and jitter tolerance. The FPM is modelled in the same manner as the downselect version.

Due to the lack of a reverse PIAA, the field PSF varies by a small amount with the core throughput decreasing by about 20% towards the edge of the dark hole. The peak PSF core throughput is 14%, the IWA is 1.3 λ_c/D, and the PSF core area is 1750 mas^2.

This design does not have a set OWA, but for the simulations presented here the dark hole was controlled over r = 1.2 - 9 λ_c/D across one-half of the field around the star due to the single DM. In an unaberrated system prior to any wavefront control the mean contrast is 9×10^{-9} from r = 1.2 - 2.2 λ_c/D and 3×10^{-9} over the full half dark hole. Running EFC on the

unaberrated system reduces the mean contrasts by nearly a factor of 10. With aberrations included and optimizing for a single polarization there is little additional degradation in contrast compared to the unaberrated case. With 0.4 mas RMS of jitter the contrast floor increased by factors of 5 - 9 near the IWA, and 1.6 mas RMS of jitter degrades contrast by nearly two orders of magnitude (Figures 10 & 11). The sensitivity measurement show that the tip/tilt tolerance is at least a few times worse than for the HLC but about the same as the characterization SPC. However, the SPC's effective jitter tolerance is greater because it is sensitive only to jitter in directions along and near the axis of the dark holes (in the perpendicular directory the SPC field stop is essentially an infinitely large occulter).

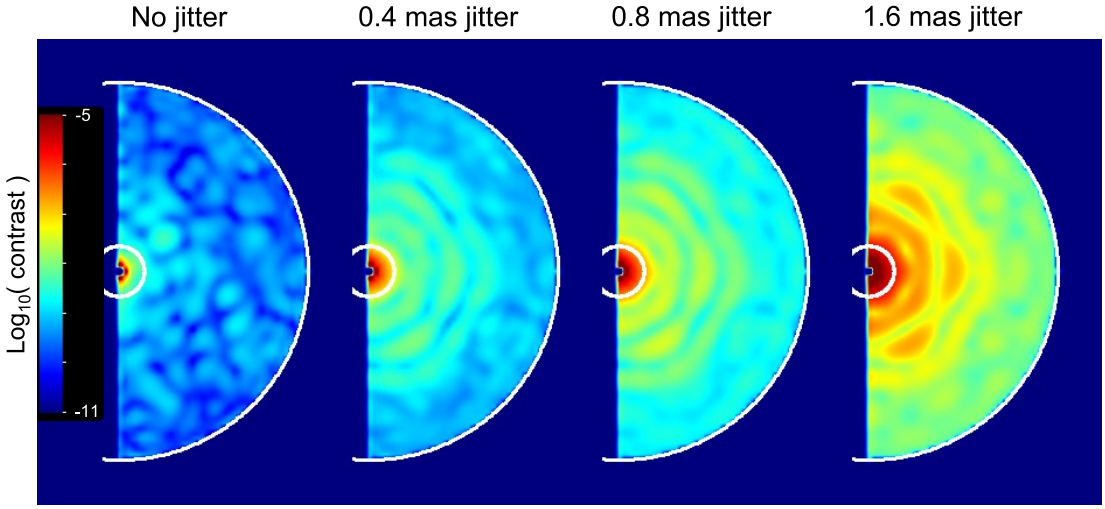

Figure 10. Revised PIAACMC contrast maps evaluated in and EFC optimized for a single polarization (λ = 523 - 578 nm; λ_c = 550 nm). Results with jitter also include a 1.0 mas star. The arcs are r = 1.2 - 9.0 λ_c/D. In color in the online proceedings.

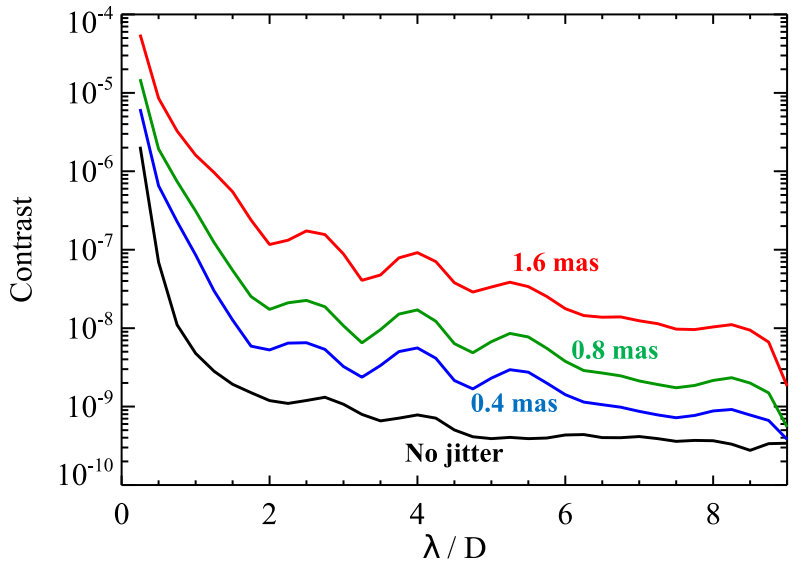

Figure 11. Revised PIAACMC (λ = 523 - 578 nm; λ_c = 550 nm) mean azimuthal contrast versus field radius with different levels of jitter and (for jittered results) 1.0 mas star evaluated in and optimized for the X polarization channel. In color in the online proceedings.

The PIAACMC astigmatism sensitivity is also about an order of magnitude greater than that for the HLC or SPC, and this reveals itself when the solution for one polarization axis is used to evaluate the contrast for the other axis. As shown in Figure 12, the unoptimized axis has contrasts levels several orders of magnitude greater than for the optimized axis. This is primarily due to the astigmatism difference between the two polarizations. A compromise solution for both polarizations would obviously have unacceptable contrast, so PIAACMC must be used in a single polarization channel at all wavelengths.

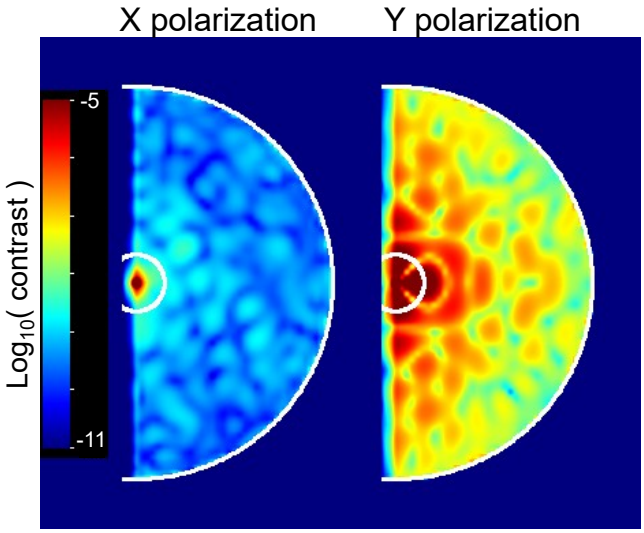

Figure 12. Revised PIAACMC contrast maps (λ = 523 - 578 nm; λ_c = 550 nm) optimized for the X polarization and evaluated in the X and Y polarization channel (no jitter). The arcs are r = 1.2 - 9.0 λ_c/D. In color in the online proceedings.

7. INTEGRATED MODELLING AND POST-PROCESSING

The AFTA optical system will not be a static structure. Besides pointing jitter from reaction wheel vibrations and FSM correction errors, the wavefront will vary over time due to thermal and structural effects as the telescope slews from target to target. Though these sub-nanometer changes may be very small by conventional definitions, they can be substantial given the sensitivity of the coronagraph. Wavefront time variations translate into speckle variations, and any lack of speckle field stability can limit the effectiveness of post-processing algorithms to extract planet signal from the complicated instrumental background.

To investigate the potential time dependences in AFTA, combined thermal, structural, and optical modelling of realistic observing scenarios have been undertaken at both the Goddard Space Flight Center (GSFC) and the Jet Propulsion Laboratory. The results presented here are for a three star imaging sequence: Begin by spending 25,000 sec on the bright star β UMa (V = 2.4, A1IV) to create/restore the dark hole, then slew to the known exoplanet host star 47 UMa (V = 5.0, G1V) for 85,000 total exposure time, and then to a reference star, 61 UMa (V = 5.3, G8V) for 85,000 sec exposures. Prior to β UMa the telescope is pointed at 61 UMa until settled. Slews take 700 sec. This scenario defined the finite element thermal modelling parameters including the heating effects from the Sun and Earth. Two versions were computed, with the Earth (geosynchronous orbit) and without (quasi-L2 orbit); the quasi-L2 orbit GSFC results are presented here. The finite element model node temperatures were computed at 5000 sec intervals and the structural element displacements, including the optical surfaces, were generated. These were then fed into ray tracing software to compute the change in the wavefront from the primary mirror up to the FSM. This delta wavefront was then inserted into the PROPER optical model. The aberration changes prior to correction for this observing scenario (named OS3) are shown in Figure 13.

Because the AFTA coronagraph has a LOWFS[10] and has correction mechanisms, their modifications to the wavefront must be included. The delta wavefront is propagated using PROPER to the FPM (for HLC or SPC) or the first Lyot stop (for PIAACMC). The reflected beam from the mask is sent into a model of the LOWFS (Zernike phase contrast sensor for HLC and SPC, or defocused image for PIAACMC) where the low order aberrations are measured, including the effects of detector noise based on the brightness of the star and the LOWFS sampling intervals (the LOWFS model was developed by Xu Wang and Fang Shi at JPL). The aberrations are sent to a model of the low order correction system developed by Erkin Sidick at JPL that includes the focus correction mechanism and the first DM (the same DM that is used to create the dark hole). The DM correction pattern is determined, including actuator gain errors, and input into the PROPER model, along with a focus correction. Uncorrected errors are propagated to the next time step.

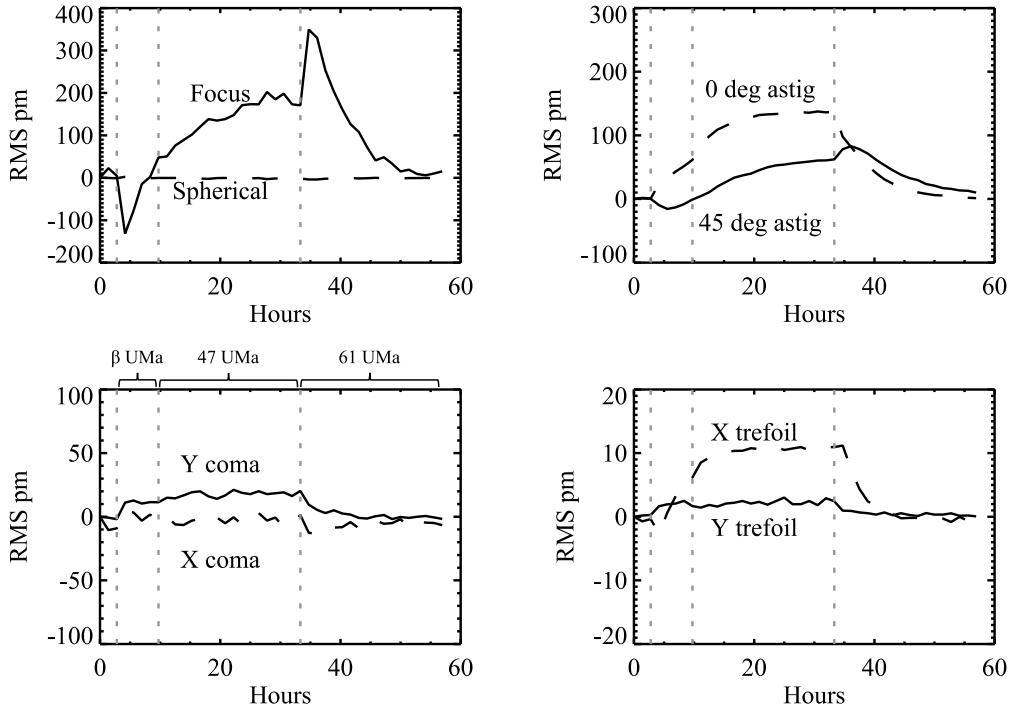

Figure 13. Low order wavefront variations over time expresses as Zernike polynomial coefficients (picometers RMS) at the plane of the FSM predicted by thermal and structural modelling for OS3 without the Earth (quasi-L2 orbit). The aberrations are referenced to time = 0 hours. The time spans spent slewing to and observing each star are indicated (prior to β UMa the system is pointed at 61 UMa).

Using PROPER and the input delta wavefronts, two time sequences of speckle fields were generated for the HLC and PIAACMC, one with low order DM correction and the other without (the DM correction has not yet been demonstrated on testbeds, so it has not yet been proven that the low order aberrations can be modified without affecting the dark hole solution). Hypothetical planets (Figure 14) were added to the 47 UMa images with different contrasts and distances from the star. In these cases we assume the dark hole has already been created prior to observing β UMa.

The simplest form of post-processing to distinguish planets from speckles is to subtract the image of one star from another, assuming that the speckles are reasonably stable over time. As a first estimate of the effectiveness of post-processing and an indicator of the stability, the images of each star were averaged together and normalized to the same intensity. The β UMa and 61 UMa images were separately subtracted from the 47 UMa one. An initial result is that there was no significant difference between the two subtractions despite the significant spectral mismatch between β UMa and 47 UMa; the speckle chromaticity is dominated by instrumental effects, not object color. The subtractions are shown in Figures 15 and 16. In the HLC two of the three planets are visible in the subtraction without DM low order correction,

and with it the third becomes visible. However, for PIAACMC none of the planets are seen in without DM correction. This is due to the increase in astigmatism during the 47 UMa observations (Figure 13) and the PIAACMC's high astigmatism sensitivity. With DM low order correction the wavefront changes are significantly reduced and all three planets are visible. More complex speckle subtraction methods can be used on these time sequences, notably those that use Principle Component Analysis[15] to optimize the combination of reference frames. These sequences are being analyzed at the Space Telescope Science Institute under contract to JPL using such advanced algorithms.

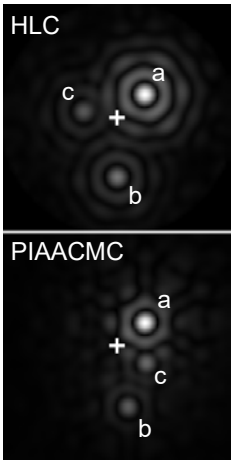

Figure 14. Test input scenes (λ = 523 - 578, λ_c = 550 nm) for the HLC and PIAACMC (including the appropriate PSFs for each field position) consisting of three planets with contrasts and apparent separations from the star of (a) 6×10^{-9} at 3.1 λ_c/D, (b) 8×10^{-10} at 5.3 λ_c/D, and (c) 9×10^{-10} at 2.9 λ_c/D.

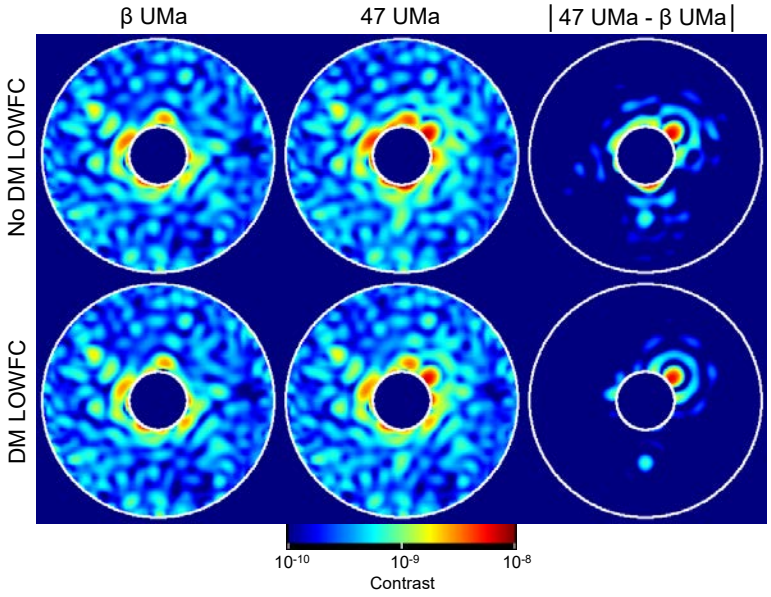

Figure 15. Averaged OS3 revised HLC dark hole fields (λ = 523 - 578, λ_c = 550 nm, single polarization) without detector noise for the bright star β UMa and science target 47 UMa (planets included) without and with low order wavefront control using the DM (focus correction is applied in all cases). The absolute differences between the two stars' fields is shown, revealing the planets. Without DM LOWFC only two planets can be seen, but with it all three can be identified. The circles are r = 2.5 & 9.0 λ_c/D. In color in the online proceedings.

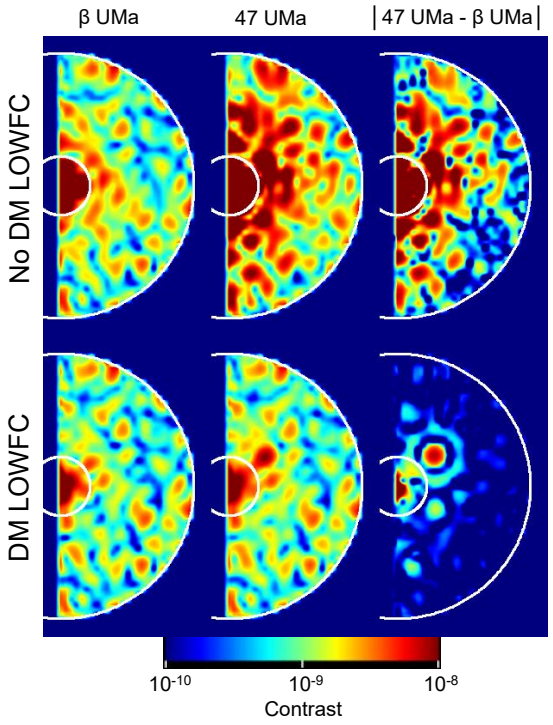

Figure 16. As with Fig. 38, but for PIAACMC (single polarization). The high sensitivity of PIAACMC to astigmatism causes the large variations in the fields between β UMa and 47 UMa when the DM LOWFC is not used. The circles are r = 2.0 & 9.0 λ_c/D. In color in the online proceedings.

8. WAVEFRONT MEASUREMENT VIA PROBING IN FINITE BANDPASSES

In the results presented so far the dark holes were generated using EFC with exact knowledge of the complex-valued image fields as directly computed using the models at multiple wavelengths. In reality the fields will be derived from intensity measurements within finite bandpasses and using DM probe patterns. Variations in the speckles within a bandpass may limit the derived field accuracy and hence the depth of the dark hole. To investigate such effects one of the authors (Zhou) has modelled the disk imaging SPC system that provides a 360° field around the star extending over 6.5 - 20 λ_c/D in a 10% (523 - 578 nm) bandpass (λ_c = 550 nm). When exact knowledge (5 wavelengths, computed field, no probing) was used with EFC, the mean field contrast is 1.3×10^{-9}.

The 10% science bandpass was divided into finite width subbands that would in reality be implemented with narrower filters. Two cases are discussed here. The first is two 5% filters within the 10% bandpass. The other is two 3.3% filters at the long and short ends of the 10% bandpass; the images from these two are subtracted from the 10% image to create a third, virtual 3.3% filter in the central wavelength range. The intensity image for each subband was created by averaging multiple simulated monochromatic fields.

Probing was done using pre-defined patterns on the DM[14]. These provided a roughly uniform offset in field intensity. The intensity changes from two pairs of DM probe patterns (positive and negative) can be used to derive the complex image plane field. The DM pattern that produces an imaginary field offset resembles a sinc function and is essentially constant over the 360° field. The pattern that creates a real offset is a double-sinc function that creates positive and negative offsets in opposing halves of the field; the points along the line separating these halves is unchanged and so the field cannot be derived there. To get around this, one can either use two pairs of real probes in perpendicular directions (in addition to the pair of imaginary probes), or use alternating directions in each EFC iteration, which is what was done here. In an unobscured system the sinc-like probe patterns are centered on the DM, but due to the obscured AFTA pupil they are offset to be centered within a clear region.

The results for the subband cases are shown in Figures 17 and 18. The 2 x 5% and 3%+10%+3% contrasts are similar and are about 2.5x worse than in the exact knowledge case. The rings of light around the inner and outer field radii are notably higher than in the exact case and are dominated by leakage at the short wavelengths of the 10% bandpass. For EFC the wavelength of each bandpass was assumed to be the central wavelength. Experiments using other assumed

bandpass wavelengths (short or long ends) for both the bandpass and in the DM response matrix used by EFC did not provide any improvement. It appears that the primary limit is lack of exact knowledge of the wavefront at the shortest wavelength. One might envision using a very narrow filter to get a more accurate estimate of the field there, but the throughput/exposure time cost would likely be too high.

It should be noted that the SPC is the least chromatic of the three AFTA coronagraphs under consideration. Similar experiments need to be run on the HLC and PIAACMC, which are much more chromatic. The current baseline design assumes that two subband filters will be available for each 10% science filter.

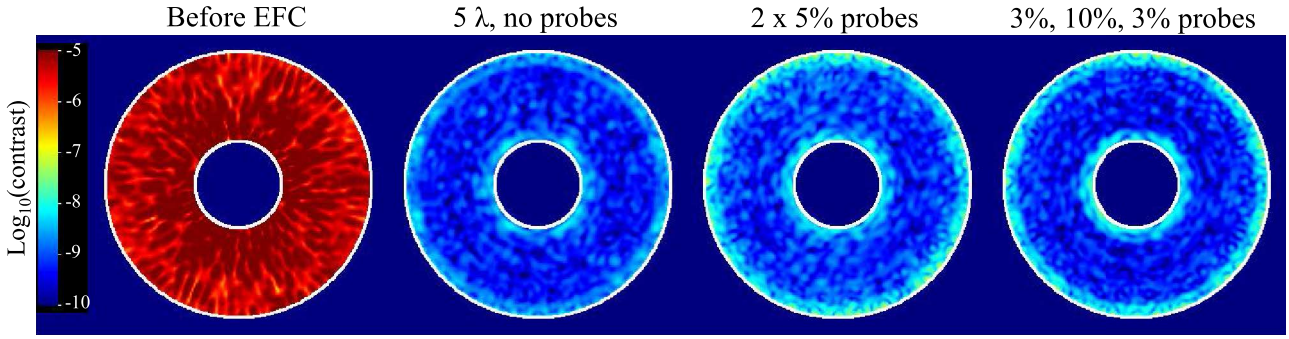

Figure 17. SPC for disks contrast maps over a 10% bandpass (λ = 523 - 578 nm, λ_c = 550 nm) for the aberrated AFTA system. The white circles are r = 6.5 and 20 λ_c/D. (Left) Before wavefront control (1.1 x 10^{-5} mean contrast). (Middle left) After EFC using the computed complex field (1.3 x 10^{-9}). (Middle right) After EFC using probing with two 5% filters (3.1 x 10^{-9}). (Right) After EFC using probing with two 3% filters and the 10% science filter (2.7 x 10^{-9}). In color in the online proceedings.

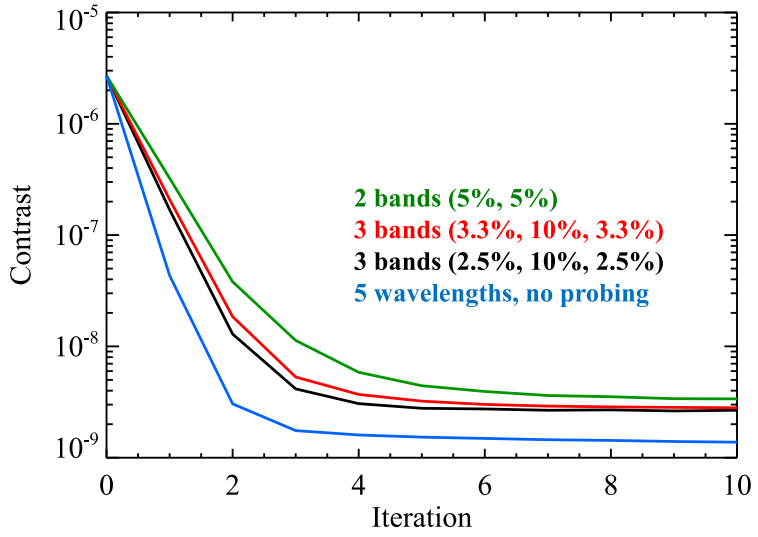

Figure 18. Mean dark hole contrast versus EFC iteration for selected sensing bandpasses for the disk SPC. The contrast is measured in a 10% bandpass over 523 - 578 nm. The "5 wavelengths, no probing" uses the computed, monochromatic, complex-valued fields, while the others use probing within finite bandpasses. In color in the online proceedings.

9. FUTURE WORK

The AFTA telescope and candidate coronagraphs form a complex optical system that has many facets to explore, both in the flight instrument design and in the ground-based testbed experiments that prove feasibility. The optical modelling group at JPL will continue to work on:

- evaluating new coronagraph designs as they become available (higher throughput, improved jitter and aberration tolerance, smaller inner working angle, increased wavelength bandwidth, etc.)
- tolerancing coronagraph components (e.g., mask fabrication errors, mask alignment requirements), including assessing how much error can be corrected using wavefront control
- additional observing scenarios for thermal modelling (rolling the telescope for angular differential imaging, longer-term IFS observation sequences)
- analyzing the impact of wavefront jitter caused by vibration of the optics by the reaction wheels
- determining the number of subbands and time required to generate dark holes in the presence of noise for each coronagraph
- and perhaps most importantly, validation of the models against testbed results.

ACKNOWLEDGEMENTS

This work was performed at the Jet Propulsion Laboratory/California Institute of Technology under contract to NASA.

REFERENCES

[1] D. Spergel, et al., Wide-Field InfraRed Survey Telescope-Astrophysics Focused Telescope Assets WFIRST-AFTA Final Report, http://arxiv.org/abs/1305.5422 (2013).
[2] J. Krist, "End-to-end modelling of AFTA coronagraphs," Proc. SPIE. 9143, 91430V (2014).
[3] J. Trauger, D. Moody, and B. Gordon, "Complex apodized Lyot coronagraph for exoplanet imaging with partially obscured telescope apertures," Proc. SPIE. 8864, 886412 (2013).
[4] A. Carlotti, N.J. Kasdin, and R. Vanderbei, "Shaped pupil coronagraphy with WFIRST-AFTA," Proc. SPIE. 8864, 886410 (2013).
[5] O. Guyon, F. Martinache, R. Belikov, and R. Soummer, "High Performance PIAA Coronagraphy with Complex Amplitude Focal Planet Masks", *Astrophysical Journal Supplement* **190**, 220 - 232 (2010).
[6] D. Mawet, E. Serabyn, K. Liewer, C. Hanot, S. McEldowney, D. Shemo, and N. O'Brien, "Optical vectorial vortex coronagraphs using liquid crystal polymers: theory, manufacturing, and laboratory demonstration," Optics Express, 17, 1902-1918 (2009).
[7] M. Shao, et al., "DAVINCI, a diluter aperture visible nulling coronagraphic instrument," Proc. SPIE. 7013, 70132T (2008).
[8] R. Lyon, B. Hicks, M., Clampin, and P. Pertrone III, "Phase-Occultation Nulling Coronagraphy," http://arxiv.org/abs/1504.05747 (2015).
[9] S. Shaklan and J. Green, "Reflectivity and optical surface height requirements in a broadband coronagraph. 1.Contrast floor due to controllable spatial frequencies," Applied Optics. 45, 5143-5153 (2006).
[10] F.Shi et al., Proc. SPIE (this volume) (2015).
[11] J. Krist, "PROPER: An optical modeling program for IDL," Proc. SPIE. 6675, 66750P (2007).
[12] http://proper-library.sourceforge.net
[13] A. Give'on, B. Kern, S. Shaklan, D. Moody, and L. Pueyo, "Broadband wavefront correction algorithm for high-contrast imaging systems," Proc. SPIE. 6691, 66910A (2007).
[14] A. Give'on, B. Kern, and S. Shaklan, "Pair-wise, deformable mirror, image plane-based diversity electric field estimation for high contrast coronagraphy," Proc. SPIE. 8151, 815110 (2011).
[15] R. Soummer, L. Pueyo, and J. Larkin, "Detection and Characterization of Exoplanets and Disks Using Projections on Karhunen-Loève Eigenimages," Astrophys. J. Letters. 755, L28 (2012).